

RESEARCH ARTICLE

10.1002/2017JE005296

Subsurface density structure of Taurus-Littrow Valley using Apollo 17 gravity data

Key Points:

- Reanalyzed data from Apollo 17 Traverse Gravimeter Experiment using modern techniques
- Results are consistent with previous analysis and place new error bounds on the data
- Investigated noise requirements for future lunar gravimetry experiments

Correspondence to:

N. Urbancic,
nurbancic@eos.ubc.ca



Citation:

Urbancic, N., R. Ghent, C. L. Johnson, S. Stanley, D. Hatch, K. A. Carroll, W. B. Garry, and M. Talwani (2017), Subsurface density structure of Taurus-Littrow Valley using Apollo 17 gravity data, *J. Geophys. Res. Planets*, 122, doi:10.1002/2017JE005296.

Received 2 MAR 2017

Accepted 1 MAY 2017

Accepted article online 5 MAY 2017

N. Urbancic¹ , R. Ghent², C. L. Johnson¹, S. Stanley^{3,4}, D. Hatch⁵, K. A. Carroll⁵, W. B. Garry⁶, and M. Talwani⁷ 

¹Department of Earth, Ocean and Atmospheric Sciences, University of British Columbia, Vancouver, British Columbia, Canada, ²Department of Earth Sciences, University of Toronto, Toronto, Ontario, Canada, ³Department of Physics, University of Toronto, Toronto, Ontario, Canada, ⁴Department of Earth and Planetary Science, The Johns Hopkins University, Baltimore, Maryland, USA, ⁵Gedex Systems Inc., Mississauga, Ontario, Canada, ⁶NASA Goddard Space Flight Center, Greenbelt, Maryland, USA, ⁷Department of Earth Science, Rice University, Houston, Texas, USA

Abstract The Traverse Gravimeter Experiment (TGE) from the Apollo 17 mission was the first and only successful gravity survey on the surface of the Moon, revealing the local gravity field at Taurus-Littrow Valley (TLV). TLV is hypothesized to be a basalt-filled graben, oriented radial to Serenitatis basin. We implemented modern 3-D modeling techniques using recent high-resolution Lunar Reconnaissance Orbiter topography and image data sets to reinvestigate the subsurface structure of TLV and constrain the volcanic and tectonic history of the region. Updated topography led to significant improvements in the accuracy of free-air, Bouguer, and terrain corrections. To determine the underlying geometry for TLV, we tested a range of possible thicknesses, dips, and wall positions for the graben fill. We found that the thickness and position previously determined by Talwani et al. (1973) represent our preferred model for the data, but with walls with dips of 30°, rather than 90°. We found large model misfits due to unmodeled 3-D structure and density anomalies, as well as parameter trade-offs. We performed a sensitivity analysis to quantify the parameter trade-offs in an ideal future survey, assuming dominantly 2-D geological structure. At the TGE survey noise level (2.5 mGal), the fill thickness was constrained to ± 150 m, the wall angle to $\pm 5^{\circ}$ and the wall positions to ± 1 km of the preferred model. This information can be used to inform the design of future lunar gravimetry experiments in regions similar to TLV.

1. Introduction

Gravity surveying allows scientists to probe the subsurface density structure of a region of interest and, in turn, reveal subsurface geologic features. Global, high-resolution (kilometer-scale) satellite gravity data are now available for the Moon from the Gravity Recovery and Interior Laboratory mission [Zuber et al., 2013]. These data have uncovered large-scale subsurface structures, including, for example, features associated with subsurface faulting around lunar impact sites [Kattoum and Andrews-Hanna, 2013]. Surface geophysical data acquired during the Apollo missions provide a unique opportunity to study the regions around lunar basins in even higher spatial resolution. Specifically, part of the Apollo 17 (A17) mission was the first lunar surface gravity survey, called the Traverse Gravimeter Experiment (TGE) [Talwani et al., 1973, hereafter T73]. The TGE measured the gravity field near Taurus-Littrow Valley (TLV), located on the southeastern rim of the Serenitatis impact basin at 20.2°N, 30.8°E.

TLV is thought to result from the formation of Serenitatis basin. Rings of ejecta concentric and exterior to the basin were crosscut by radial normal fault-bounded troughs (graben), one of which formed the TLV (Figure 1). At a later time, this graben was flooded with basalt, likely after some degradation by mass wasting had already taken place. Ejecta material on the northern and southern flanks of the valley formed the North and South Massifs (NM and SM), as well as other smaller mountains to the east (e.g., sculptured hills (SH) and family mountain (FM)) that are mainly composed of brecciated highland material [Wolfe et al., 1981; Schmitt et al., 2016].

The TGE data set was first analyzed by T73, with simple 2-D corrections to the gravity data and models for the region, yielding an approximate depth extent for the valley fill of 1.0 km. This places a constraint on the

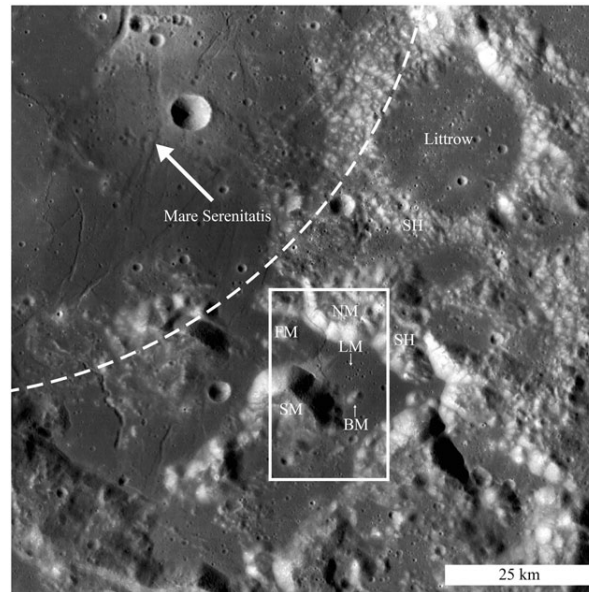


Figure 1. LROC Wide-Angle Camera (WAC) mosaic [Robinson *et al.*, 2010] for Taurus-Littrow Valley (TLV) (rectangle), southeastern side of Serenitatis basin (dashed line) and surrounding region. The image field of view is approximately 100 km wide and the image resolution is 100 m/pixel. LM = Lunar Module landing site (20.19080°N, 30.77168°E), SM = South Massif, NM = North Massif, SH = Sculptured Hills, FM = Family Mountain, BM = Bear Mountain. For reference, 1° of latitude is 30.3 km.

volume of lava extruded at the time of formation. Recent, high-resolution Lunar Reconnaissance Orbiter Camera (LROC) Narrow-Angle Camera (NAC) Digital Terrain Models (DTMs) [Oberst *et al.*, 2010], as well as LROC NAC and Wide-Angle Camera (WAC) images [Robinson *et al.*, 2010], can improve the accuracy of data corrections, georeferencing, and modeling.

This analysis is motivated by three goals. First, we update the data processing done by T73 using high-resolution DTMs and 3-D correction methods, and we assess the effect of these updates on the amplitude of corrections to the gravity measurements (free air, Bouguer, and terrain). We also quantify the corresponding uncertainties in the corrections. Second, we investigate whether the updated processing allows us to extract new information about the 3-D subsurface structure of TLV and thus constrain the volcanic and tectonic history of the region. Third, we compute a series of forward models to quantify parameter

trade-offs that are present at different noise levels for an idealized 2-D geological environment. These results can guide the design of future surface gravity experiments.

2. Traverse Gravimeter Experiment

2.1. Data

The Apollo 17 astronauts took measurements of the vertical gravity on and off the rover during the three extravehicular activities in TLV. Measurements taken on the lunar rover were more convenient but were susceptible to vibrations generated by the vehicle. In total, 25 successful measurements were recorded at 12 locations: stations 2, 2A, 3, 4, 5, Apollo Lunar Surface Experiment Package (ALSEP), 1, Lunar Module (LM), Surface Electrical Properties (SEP), 6, 9, and 8 (in order of increasing distance across the valley). The average station spacing was about 1 km.

Of these measurements, T73 used five measurements at the LM to determine the absolute gravity at the landing site and for various instrumental calibration purposes, such as periodic thermal monitor readings, and to ensure proper functioning throughout the survey. Repeated off-rover measurements were taken at the LM and at stations 8 and 9 to calibrate the on-rover measurements and to quantify the gravimeter drift and noise. T73 took a series of off-rover measurements at the LM site. The instrumental noise was calculated from the root-mean-square (RMS) value of the measurements minus the first measurement value. No systematic instrumental drift was observed. An empirical correction of -6.0 mGal was made to each station's on-rover measurements to account for an average bias relative to the off-rover measurements (T73).

We georeferenced the TGE data set to determine measurement locations. This step was performed manually by aligning hand-drawn maps to previously georeferenced Lunar Reconnaissance Orbiter Camera (LROC) Narrow-Angle Camera (NAC) images (resolution of ~ 0.5 m/pixel) [Robinson *et al.*, 2010]. The uncertainty in our georeferencing was ± 5 m, and this translates into an error in the gravity corrections and modeling of less than 0.25 mGal. Figure 2 shows a LROC NAC digital terrain model (DTM) [Oberst *et al.*, 2010] for TLV, along with the location of the stations and the line "T" used in T73 for corrections and modeling. Station gravity measurements relative to the LM are listed in Table 1 taken from Talwani [2003] and are shown as a function of position along line "T" in Figure 3.

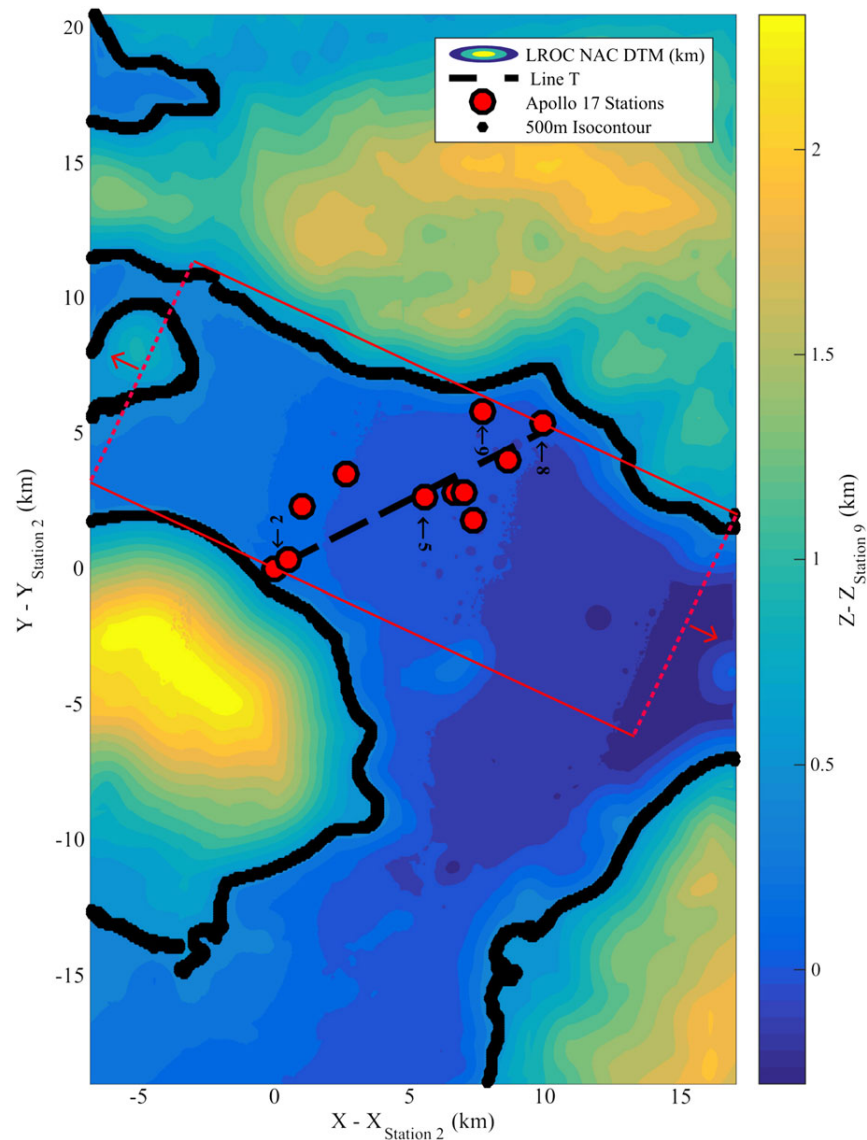


Figure 2. LROC NAC DTM [Oberst *et al.*, 2010] for TLV (see rectangular region in Figure 1), with station locations (red circles), the boundary between valley and massifs, defined as the 500 m isoline separating different density regions (solid black lines), the line “T” (dashed black line) used for the 2-D analysis in T73, and the modeled subsurface region in this study (red rectangle-dashed red lines; the arrows indicate that the model region has a total length of 30 km that extends beyond the figure boundaries).

2.2. Corrections

T73 analyzed the TGE data by projecting the data on to a line (named “T” here) roughly perpendicular to the valley. All of the corrections and modeling then were performed along this line. In order to isolate any contribution to the measured gravity from the subsurface mass distribution, one must also take into account the gravitational effect of differences in measurement height from a common elevation baseline and the corresponding mass above that baseline. Gravity corrections typically applied are the free-air correction, Bouguer correction, and the terrain correction.

The free-air correction accounts for the change in gravity with radius from the Moon. The rate of change is given by equation (1) and has a value of 0.19 mGal/m, where G is the gravitational constant, M_m is the mass of the Moon, r is the radius of the Moon taken to be the lunar reference radius of 1737.4 km [Archinal *et al.*, 2011],

Table 1. Traverse Gravimeter Experiment Data

Station Name	Distance Along Line T ^a (m)	X ^a (m)	Y ^a (m)	$\Delta Z_{\text{LROC}}^{\text{b}}$ (m)	$\Delta Z_{\text{T73}}^{\text{c}}$ (m)	Δg_z^{d} (mGal)
2	0	3	-6	207	110	-50.8
2A	590	519	283	196.9	90	-40.5
3	1,854	1,014	2,262	152	50	-16.5
4	3,885	2,674	3,516	110	28	-4.5
5	6,176	5,589	2,613	63	10	-10.6
ALSEP	7,283	6,703	2,830	32	-5	-1.3
1	7,386	7,304	1,745	20	-5	-4.6
LM	7,420	6,876	2,781	28	-5	0.0
SEP	7,549	7,006	2,805	28	-5	-3.7
6	9,389	7,686	5,775	88	60	-36.0
9	9,520	8,641	3,968	0	0	-12.7
8	11,256	9,910	5,376	34	60	-31.6

^aMeasurements are taken with respect to station 2's projected position along line T. Station locations have a ± 5 m uncertainty derived from LROC NAC images [Robinson *et al.*, 2010].

^bLROC NAC DTM elevation with respect to the reference elevation at station 9 [Oberst *et al.*, 2010], with a 2 m horizontal resolution and a 2.05 m vertical error.

^cElevation measurements from T73, with a 500 m horizontal resolution.

^dGravity measurements taken from T73, relative to the LM. Instrumental uncertainty on gravity measurements is ~ 1.8 mGal (T73).

and g_{Moon} is the gravity of the Moon. The free-air correction is the product of the rate given by equation (1) and the elevation at the measurement location.

$$\frac{\partial g_m}{\partial r} = \frac{-2GM_m}{r^3} = \frac{-2g_{\text{Moon}}}{r} \quad (1)$$

In T73 a satellite-derived DTM was used, with approximately 500 m horizontal resolution, to correct all of the measurements to a datum, which was taken to be the elevation of the lowest station, the LM. In this study we used the LROC NAC DTM (2 m horizontal resolution and 2.05 m vertical error) within 20 km of each station, and the LRO LOLA DTM (smoothed to 40 m horizontal resolution) outside of 20 km. The vertical error for the LROC NAC DTM was derived from the RMS difference between the Lunar Reconnaissance Orbiter's (LRO) Lunar Orbiter Laser Altimeter (LOLA) elevation measurements [Zuber *et al.*, 2010] and the LROC NAC DTM [Oberst *et al.*, 2010]. In our case we took the reference elevation to be that of station 9 instead of the LM because station 9 had a lower elevation than the LM using the LROC NAC DTM. The elevation profiles relative to station 9, along line T, from the DTM used in T73 (black), and the LROC NAC DTM (red) are shown in Figure 3a. The free-air correction is linearly related to the elevation, and so the 100 m change in elevation between T73 and the LROC NAC DTM at station 2 corresponds to a ~ 20 mGal increase in the amplitude of the free-air correction (see Figure 3b).

Figure 3c shows the combined Bouguer slab and terrain correction (CBT), which is used to account for the mass between the topography and the chosen datum at the station locations. Typically, in low-relief cases the mass is sufficiently accounted for using the infinite Bouguer slab correction, assuming an average density and height for the region. However, a terrain correction is necessary in situations where the range in topographic relief around the stations is large. TLV meets this criteria, as the stations are located close to high relief mountains.

In the case of TLV, we have some knowledge of the material properties and their spatial distribution in the valley. Based on the distributions of Apollo sample density values presented in Table 13 of T73, and using the spread in measured values to derive uncertainties, we use the following structure. In the valley below the 500 m isoline in Figure 2, there is basaltic material with a density of approximately 3.2 ± 0.2 g/cm³, and the massifs above the 500 m isoline are brecciated highland rock with a density of approximately 2.4 ± 0.2 g/cm³. Because of the heterogeneous density distribution in TLV, we used a spatially dependent, two-component density model when computing both the Bouguer and terrain corrections, instead of using a single,

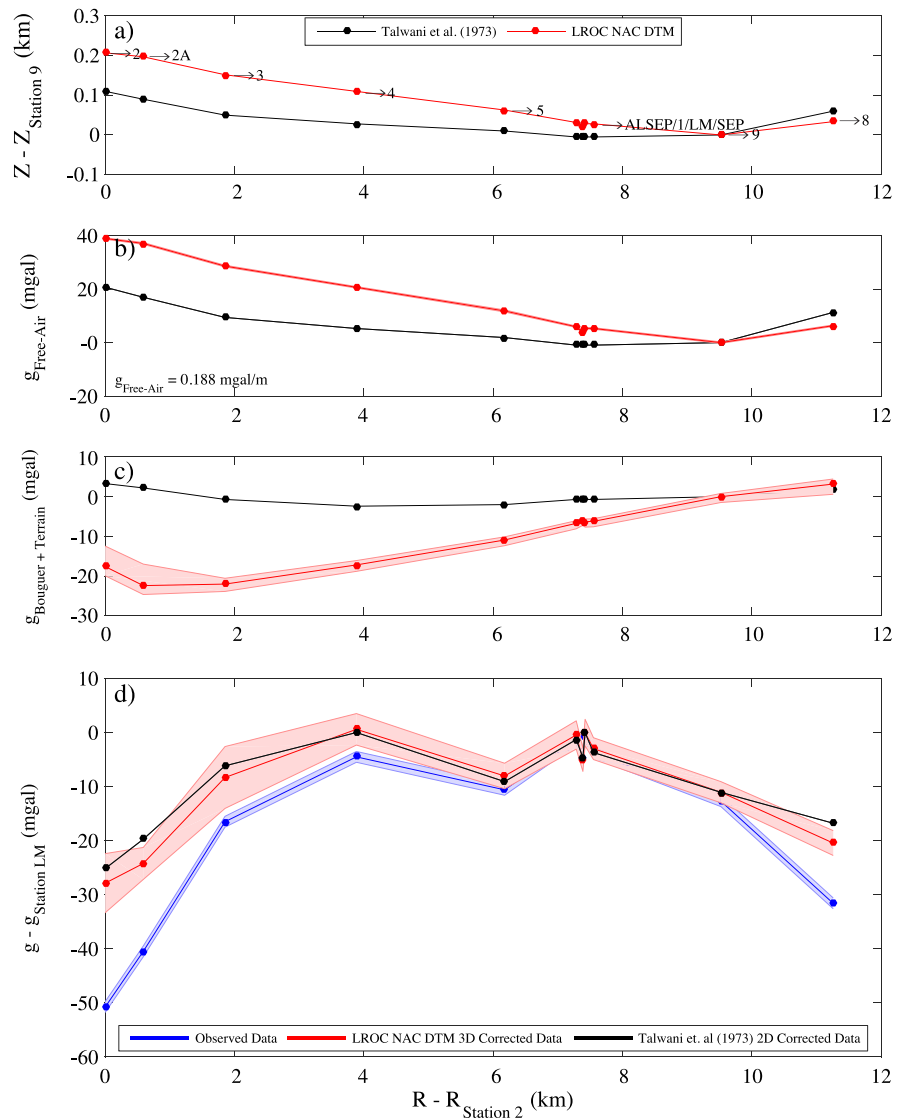


Figure 3. (a) LROC NAC DTM elevation measurements used in our analysis (red) compared to elevation measurements used in T73 (black), (b) free-air corrections, (c) combined Bouguer and terrain correction, and (d) corrected gravity values with respect to the lunar module (LM) and original uncorrected data (blue). All profiles in Figures 3a–3d are shown as a function of distance along line “T” (Figure 2) relative to station 2. Station 6 has been removed due to projection issues. Measurements and corrections in Figures 3a–3c are adjusted to be relative to station 9. Uncertainties on the original uncorrected data in Figure 3d are 1.8 mGal (Table 1 and text). Uncertainties in the free-air (Figure 3b), combined Bouguer, and terrain correction (Figure 3c) and the resulting corrected data (Figure 3d) are detailed in the text.

average density. Depending on the location of the density boundary assumed, the CBT corrections have a maximum variation of $\pm 5_2$ mGal, which we have included in the uncertainty on our profiles shown in Figures 3c and 3d.

To implement the two-density model for the region, we used a finite slab (instead of a single density infinite slab that is often used for the Bouguer correction), which is made up of a series of flat faced 3-D prisms [Parasnis, 1986; Nagy, 1966], each with an assigned density ρ , with a fixed upper surface at the station elevation, a lower surface at the reference elevation at station 9, and a width equivalent to the DTM resolution. The choice of reference elevation in computing the corrections was investigated and found to contribute a negligible amount to the measured gravity, specifically less than 0.15 mGal for a 10 km radius around each station.

Table 2. Corrections

Station Name	T73 Free Air ^a	Updated Free Air ^b	T73 Bouguer and Terrain ^c	This Study Bouguer and Terrain ^d	T73 $\Delta g_{\text{corrected}}$ ^a	This Study $\Delta g_{\text{corrected}}$ ^b
2	20.7	38.9	3.3	-17.6	-25.2	-27.9
2A	16.9	37.0	2.2	-22.4	-19.7	-24.2
3	9.4	28.5	-0.7	-22.0	-6.2	-8.3
4	5.3	20.6	-2.4	-17.2	0.0	0.6
5	1.9	11.8	-2.0	-10.9	-9.1	-8.0
ALSEP	-0.9	5.9	-0.7	-6.7	-1.3	-0.4
1	-0.9	3.8	-0.7	-5.9	-4.6	-5.0
LM	-0.9	5.3	-0.7	-6.3	0.0	0.0
SEP	-0.9	5.3	-0.7	-6.2	-3.7	-3.0
6	-	16.6	-	-4.5	-	-22.2
9	0.0	0.0	0.0	0.0	-11.1	-11.0
8	11.3	6.3	1.9	3.2	-16.8	-20.4

^aFree-air correction values taken from T73, calculated using elevations from satellite-derived DTMs (T73) presented in Table 1. Values have been adjusted for a baseline of station 9.

^bFree-air correction values from this study, calculated using elevations from LROC NAC DTM [Oberst *et al.*, 2010] presented in Table 1.

^cCombined Bouguer and terrain correction values are taken from T73, calculated using elevations from satellite-derived DTMs (T73) presented in Table 1 and using 2-D prisms [Talwani *et al.*, 1959]. Combined Bouguer and terrain corrections have been adjusted to be relative to station 9.

^dCombined Bouguer and terrain correction values from this study, calculated using elevations from LROC NAC DTM [Oberst *et al.*, 2010] presented in Table 1 and using 3-D prisms [Parasnis, 1986; Nagy, 1966]. Combined Bouguer and terrain corrections have been adjusted to be relative to station 9.

^eCorrected gravity values taken from T73. Corrected gravity values have been readjusted to be relative to the LM.

^fCorrected gravity values from this study. Corrected gravity values have been readjusted to be relative to the LM.

For the terrain correction we computed the gravity at each station by also summing the contributions from a series of prisms which represent the difference in mass between the DTM and a flat surface at the elevation of the current station. Our grid cell sizes in the terrain correction calculation were 2 m per pixel (the resolution of the NAC DTM) within 500 m distance of each station. We increased the cell size beyond this distance, following the inverse square dependence of gravity on distance; i.e., if the distance doubles, the prism area can be quadrupled. We computed the terrain correction for the two stations, 2 and 8, closest to the massifs at the full resolution of the LROC NAC DTM and verified that our variable cell size algorithm gave negligibly different results. We extended our integration to a radius at which the gravity contribution was negligible. This radius was determined from convergence tests to be ~ 170 km.

The shape, size, and extent of these prisms affect the accuracy of the correction. However, we found that using 3-D, flat-topped square prisms was sufficiently accurate, because the stations are on relatively flat terrain, and the highest slope regions are farther away. The vertical gravity g_{prism} due to a single prism of density ρ is given by summing the contributions from eight vertices of a parallelepiped, where each vertex has coordinates (x_i, y_j, z_k) , where $r = \sqrt{x_i^2 + y_j^2 + z_k^2}$. Thus,

$$g_{\text{prism}} = G \sum_{i,j,k=1,2} \rho (-1)^{i+j+k-1} f(x_i, y_j, z_k) \quad (2)$$

$$f(x_i, y_j, z_k) = \left[x_i \ln \frac{y_j + r}{\sqrt{x_i^2 + z_k^2}} + y_j \ln \frac{x_i + r}{\sqrt{y_j^2 + z_k^2}} + z_k \tan \left(\frac{z_k r}{x_i y_j} \right) \right] \quad (3)$$

In the T73 study, the Bouguer and terrain corrections were combined and calculated using 2-D prisms [Talwani *et al.*, 1959]. T73 assumed a multidensity distribution in 2-D, with a boundary similar to that in our analysis, and they performed their 2-D correction along line T, extending approximately 10–15 km beyond the outermost stations along line T.

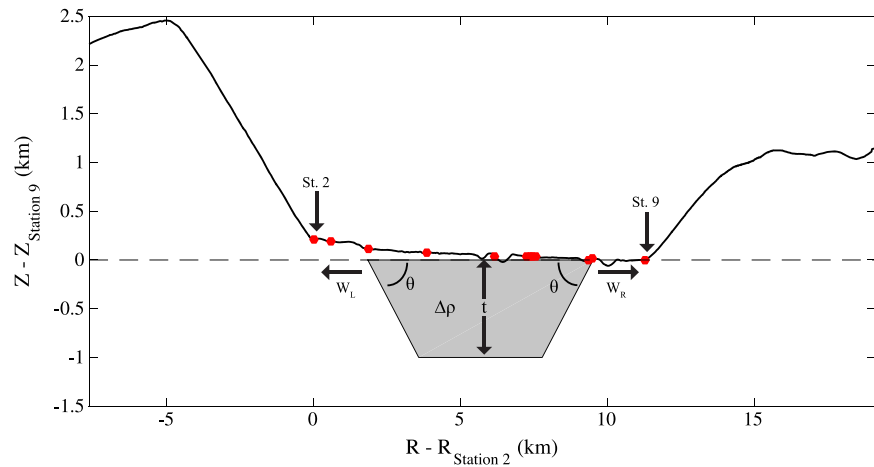


Figure 4. LROC NAC DTM elevation along line T, and cross section of model of the valley. See section 3.1 for parameter definitions.

The CBT corrections can be seen in Figure 3c. Differences between our CBT and the T73 corrections are partly related to the elevation difference between our LROC NAC DTM and T73. By updating the elevation map, increasing the radius of integration by almost an order of magnitude, and performing the correction in 3-D (instead of 2-D) we found nonnegligible CBT corrections with a magnitude of up to ~ 20 mGal.

The corrected data curves are shown in Figure 3d. The individual corrections at each station and the final corrected values are listed in Table 2. The uncertainty on our corrected curve was derived from the instrumental uncertainty (1.8 mGal), the accuracy in the elevation model (~ 2.05 m), uncertainties derived from the range of possible densities (± 0.4 g/cm³) and the spatial distribution of those densities (± 5 mGal), and the positional uncertainty on measurement locations. To quantify the uncertainty that station locations have on the gravity profile, we computed the maximum slope in the gravity profile across line T for a suite of models, with a value of 0.05 /m. For a station location uncertainty of ± 5 m, this converts to a maximum uncertainty of 0.25 mGal. Including these sources of error results in an average uncertainty per station of 2.5 mGal. The uncertainties are largest on the western end of the profile due to the close proximity of stations to the South Massif. It is evident that although the accuracy of the individual corrections are significantly improved by using a new high-resolution DTM for the region and performing corrections in 3-D, the final corrected curve agrees well with the corrected curve in T73. The curve has a similar shape to T73, but a slightly larger amplitude.

3. Modeling

3.1. Valley Geometry

TLV is roughly linear and the cross-section geometry [Ryder *et al.*, 1992] can be described by four parameters (Figure 4). The valley wall positions, W_L and W_R (referred to below as the wall positions), describe the distance between the outermost stations along line T and the maximum lateral extent of the subsurface basalt. The valley thickness, t , describes the thickness of the subsurface basalt fill. The angle, θ , describes the dip of the graben walls. From conventional faulting theory, we expect this angle to be close to 60° [Thatcher and Hill, 1991]. However, an extended time period between the graben formation and the basalt infill was likely [Wolfe *et al.*, 1981], and thus, we expect the angle to have shallowed through mass wasting toward its angle of repose, and possibly beyond this angle by impact gardening and seismic shaking by impacts [Fassett and Thomson, 2014; Kreslavsky and Head, 2016].

3.2. Previous Models

T73 performed forward modeling of the gravity for a series of 2-D rectangles ($\theta = 90^\circ$ in Figure 4) for various thicknesses and wall positions. They assumed a density contrast of 0.8 g/cm³, reflecting the assumed difference between the basaltic material and the background brecciated highland rock material. The resulting preferred model has a thickness $t = 1$ km and wall positions $(W_L, W_R) = (2, 0)$ km, hereafter referred to as (2, 0) km (Figure 5). It is clear that although their preferred model roughly matches the width and amplitude of the corrected data curve, the slopes at the edges of the model curve do not fit the observed corrected profile.

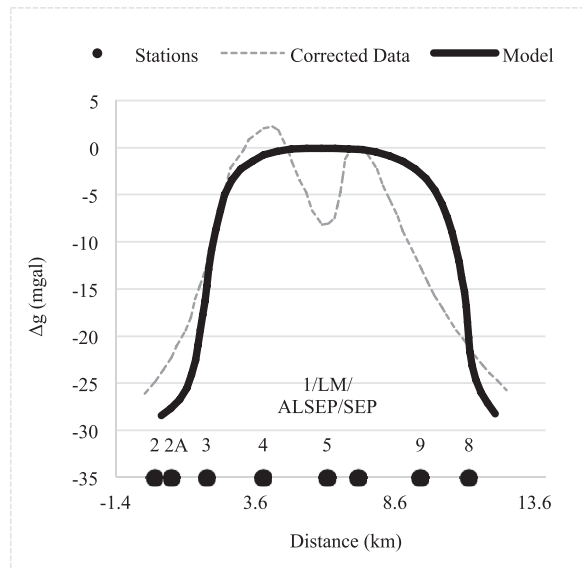


Figure 5. Corrected gravity profile along line T (dashed black line) as well as the gravity profile from the preferred model (solid black line) from T73.

than 5 km to the south of station 2's projected location (for $Y - Y_{\text{station2}}$ less than -5 km in Figure 4) produces less than 1.5% change in the model gravity at all station locations. Thus, this southern section of TLV was excluded from modeling to reduce computation time. The resulting model region is a linear valley that can be described by a roughly NW-SE strike (Figure 2), and thus, we treated it as having a fixed subsurface cross-sectional geometry extending along the length of the valley.

T73 generated 2-D models that assumed an infinite strike perpendicular to line T. This approximation typically requires the length perpendicular to the cross section to be roughly 20 times the next largest dimension [Lowrie, 2007]. In the case of TLV, the cross-section width, measured along line T between stations 2 and 9, is ~ 9 km and the valley extends up to ~ 30 km in the NW-SE direction (Figure 2), only ~ 3 times the width. Additionally, line T is oriented at $\sim 63^\circ$ E from north, and thus, T73 modeled the valley with a strike of 153° . From the LROC NAC DTM, we estimated an average orientation of $\sim 115 \pm 25^\circ$ and used the average strike of 115° in our model (cf. $\sim 153^\circ$ in T73), noting that line T is not perpendicular to the valley in this case.

The density contrast for our models were taken to be the same as in T73 ($0.8 \pm 0.4 \text{ g/cm}^3$) and as used in our corrections, reflecting the difference between basalt ($3.2 \pm 0.2 \text{ g/cm}^3$) and the background brecciated highland rock material ($2.4 \pm 0.2 \text{ g/cm}^3$). The 50% uncertainty on the density contrast, $\Delta\rho$, is based on the large spread in density measurements, likely due to inhomogeneity within each rock type, measured for basalt and brecciated highland rock material recorded in T73. We have not included this density uncertainty in our models but refer to its effects in the discussion section.

We investigated a suite of different model parameter combinations. Guided by the results in T73, we first computed the gravity at the stations for vertical-walled ($\theta = 90^\circ$) models with various wall positions of 0, 1, and 2 km from the outermost stations, measured in units of distance along line T, and thicknesses of 0.8, 0.9, 1.0, 1.1, and 1.2 km. Second, we varied the wall angles from 30° to 90° in 15° increments, allowing the wall positions to also vary from 0 to 2 km but fixing the fill thickness to the value obtained for the best fitting 90° model (1 km).

Figures 6a–6c show example model fits. In Figure 6a, the wall positions are fixed at (2, 0) km and the thickness is varied. In Figure 6b, the thickness is fixed as 1 km, but the wall positions are varied; in both Figures 6a and 6b, the wall angle is fixed at 90° . In Figure 6c, the wall position and thickness are fixed at (2, 0) km and 1 km, respectively, and the predictions of models with our end-member wall angles of 30° and 90° are shown. Differences among model profiles for intermediate wall angles (e.g., 45° , 60° , and 75°) are less than the uncertainty in the observations.

Additionally, there is also a substantial negative anomaly located at station 5 which is unexplained by the T73 model. However, it is unclear whether the station 5 anomaly is significant because of projection effects from the 2-D analysis, the coarse spatial resolution of the survey, unequal measurement spacing, and unmodeled local density variations in the lunar crust.

3.3. Updated Models

We generated 3-D shape models of the subsurface using ModelVision software (Software for PC developed and supported by Tensor Research Pty Ltd. (2014). ModelVision Version 14. PO Box 5189, Greenwich, New South Wales 2065, Australia) and varied the four geometric parameters from Figure 4 (W_L , W_R , t , and θ) to control the geometry of the cross section along line T. Tests showed that including structure, more

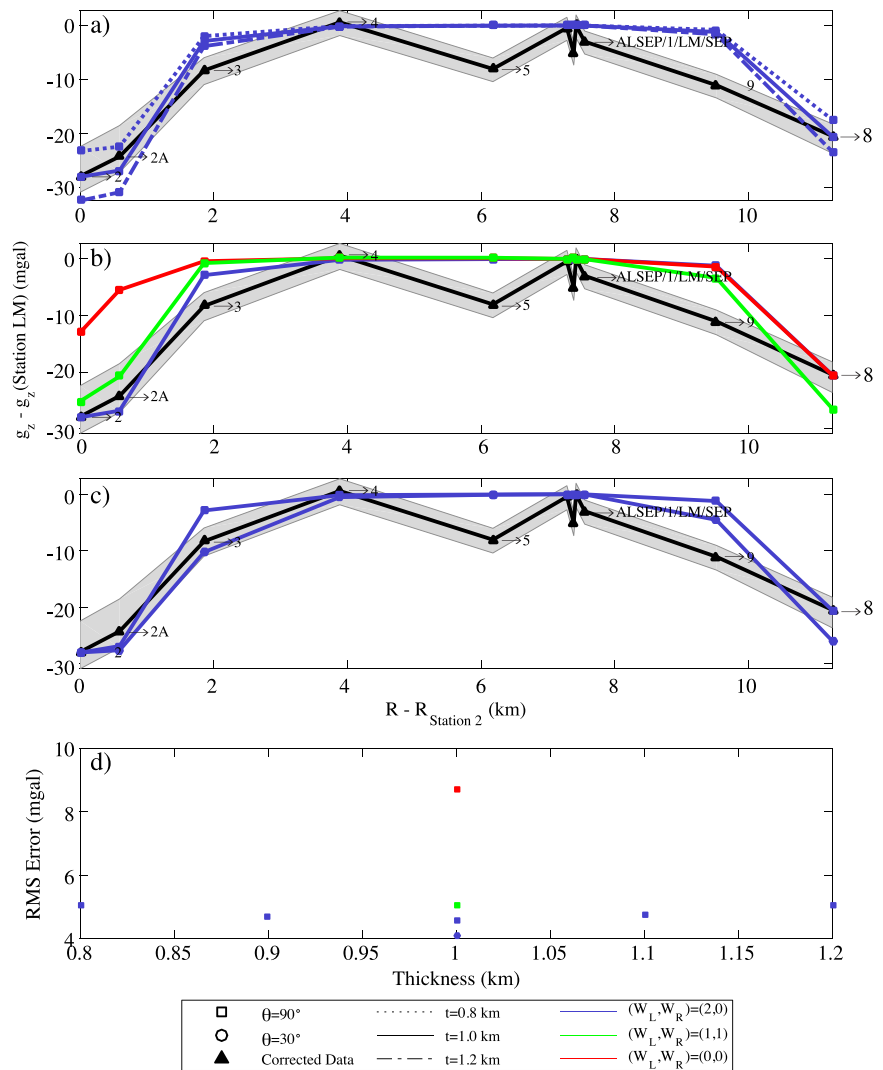


Figure 6. Vertical-walled models ($\theta = 90^\circ$) are represented by squares, and angled-wall ($\theta = 30^\circ$) models are represented by circles (only shown in Figure 6c). The line types indicate different fill thicknesses and colors represent wall positions. The corrected data profile is shown in black with the uncertainties denoted by the gray shaded region. (a) Gravity generated from 2-D rectangular models, with a wall position of (2, 0) km and various thicknesses. (b) Gravity generated from 1 km thick, rectangular models, for different wall positions. (c) Gravity generated from 1 km thick, rectangular model and 30°-angled-wall model, both with wall positions of (2, 0) km. (d) RMS difference between model and data for models with various thicknesses, wall positions, and wall angles.

As expected, increasing the thickness of the basaltic fill increases the overall amplitude of the model signal (Figure 6a). We found that it was difficult to find a match to the shape of the observed profile for any single wall position. Assuming model wall positions of (1, 1) km qualitatively approximates the slope of the left-hand side, but not the right-hand side of the observed profile (Figure 6b). It also has the incorrect amplitude. In contrast, model wall positions of (2, 0) km visibly matches the amplitude but has a steeper slope on the left-hand side of the profile (Figure 6b) than the data.

Changing the wall angle for the (2, 0) km wall positions results in differences in behavior for the western and eastern edges of the profile. These occur because of (i) the different wall positions and (ii) the uneven spacing of the stations along profile T. For a wall position of (2, 0) km, stations 3 and 8 are at the edges of the mass anomaly. As the wall angle shallows from 90° to 30°, the gravity values at the stations at the edge of the valley fill are reduced (due to the decreased positive mass anomaly beneath the stations). The gravity profile falls off less steeply outside the outer limits of the valley fill (i.e., between stations 1 and 2 and station 3 on the western

edge of the valley); however there are no such station locations on the eastern edge of the profile and so this behavior is not observed. The decreased wall angle means that the model gravity profile now increases from stations 3 and 8 toward the center of the valley (i.e., between stations 3 and 4 and between stations 8 and 9). On the western side of the profile, for a wall angle of 30° , the full fill thickness is reached by station 4 and so the amplitude of the model gravity profile is close to the peak amplitude here. On the eastern edge of the profile the full fill thickness is reached between stations 8 and 9 and so the first station for which the model-predicted amplitude is close to the peak amplitude is station 9. All models result in a poor fit at station 9, independent of wall position. It is likely this side of the profile reflects subsurface structure that is not being captured by the simple geometry of our models.

In order to determine our preferred model, we computed the RMS difference between the corrected data profile and each model profile (Figure 6c). The RMS misfit was found to be relatively insensitive to fill thickness, over the range of plausible thicknesses tested (Figure 6c). Furthermore, the thickness trades off directly with the density contrast, for which we have a 50% uncertainty. Thus, it is very difficult to determine the correct model thickness in the presence of large density uncertainties. In comparison, incorrect wall positions lead to relatively large range in RMS misfits which gives us better sensitivity to determining the wall position. Using our assumed density contrast and vertical walls ($\theta = 90^\circ$), the preferred model has wall positions of (2, 0) km and a thickness of 1 km, in agreement with the preferred model parameters in T73, as shown in Figure 5. The RMS misfit changes by only 0.5 mGal for wall angles from 90° to 30° (Figure 6d), indicating a weak sensitivity to the wall angle. The lowest RMS model parameters correspond to wall positions of (2, 0) km, a thickness of 1 km and an angle of 30° .

4. Discussion

Our 3-D models show that for the parameters and parameter ranges searched, the wall positions are the parameters that exert the dominant control on the misfit. For example, for wall positions not close to the optimal value, the RMS misfits can be large (~ 9 mGal for wall positions of (0, 0)). For a given thickness and wall angle, the optimum wall positions are (2, 0). Tests showed that all wall positions of (1, 0) for a comparable thickness and wall angle gave RMS misfits typically only ~ 0.1 – 0.3 mGal worse. For the optimal wall positions there is only a weak sensitivity to wall angle and thickness and the best RMS misfit (4.1 mGal for thickness of 1 km and dip of 30°) is still greater than the average uncertainty in the corrected data profile (~ 2.5 mGal). For this model (the “preferred model”), deviations of the data from the model at individual stations can be large, e.g., at station 5. The results indicate that discrepancies between model and the data are related to structure not present in our simplified physical model.

Thus, rather than investigate trade-offs among parameters in our simplified model further, we first discuss possible physical origins of additional subsurface structure that may contribute to the observed gravity profile (section 4.1). We then assume a simple 2-D valley geometry and investigate the trade-off space among model parameter uncertainties that might be expected from future surveys in such geological settings (section 4.2). This is done by producing synthetic data for a suite of models and comparing them to synthetic data generated for an assumed underlying infinite 2-D geometry with a strike of 153° , wall positions of (2, 0), thickness of 1 km, and angle of 30° . We use the results to determine the sensitivity to fitting various model parameters at different noise levels in the absence of complicated surface and subsurface geometries and to quantify the noise levels required to constrain model parameters for future lunar gravimetry studies.

4.1. Additional Subsurface Structure

The 3-D preferred model for TLV describes the majority of the measurements taken at TLV, but a few large discrepancies between the model and data indicate the presence of additional structure not captured by this simple model. For example, the floor of TLV is not flat throughout the valley as assumed in our model. There are many mechanisms that could produce this including parts of FM and the NM protruding through the valley floor, Tycho ejecta emplaced onto the valley floor [Lucchitta, 1977], and surface tilting resulting from listric faulting at the time of graben formation. Listric faulting could also generate multiangle walls, instead of the single angle walls we have assumed.

Motivated by some anomalies at individual stations, we can also look for local surface structure not captured by our models. Specifically, Figure 2 shows that station 9 is located closest to a portion of the TLV wall where the local strike of the valley wall is quite different from the average strike assumed in our models. In addition, the wall dip at stations 8 and 9 may be different as they correspond to different segments of the valley wall.

The floor may not be flat in this intersection region of the North Massif and the Sculptured Hills. Thus, the apparent gravity anomaly at station 9 could be explained by modeling these complex geometries. To deal with the incorrect strike for station 9, one could generate 3-D models using the shape of the perimeter of the valley instead of a single finite linear strike. However, models for multiangle walls and a nonflat floor in this region would be heavily unconstrained.

One other feature that none of the models predict is the negative anomaly in the corrected gravity profile at station 5 (-8.0 mGal). The amplitude of the anomaly is -8.0 mGal with respect to the LM (0.0 mGal), and -8.6 mGal with respect to station 4 (Figures 6a–6c). The ALSEP and SEP stations are within 200 m radius of the LM (ALSEP = 179 m and SEP = 133 m) and their corrected gravity values are -0.4 and -3.0 mGal, respectively, compared to 0.0 mGal at the LM (Figure 3c). The mean of these values gives us an estimate of the local variability around the LM with a value of -1.1 ± 1.6 mGal. If we take this local variability into account, the maximum amplitude of the anomaly relative to the neighboring stations (LM, ALSEP, and SEP) at station 5 is -6.9 ± 1.6 mGal.

There are multiple clear, easily modeled, surface and subsurface mass anomalies that could generate this gravity anomaly. Surface mass anomalies may have been generated by the terrain correction performed in section 2.2, as everything below the station 9 baseline is assumed to be a homogeneous slab of either basalt or highlands material, depending on the location. Therefore, topographic features such as craters that extend partially below the station 9 baseline have artificially been assumed to be filled with basalt below this baseline. We examined the surface geology around station 5 to look for any large features that are below the baseline. One example is Camelot crater, located ~ 50 m from station 5 (measured from the edge of Camelot). The crater has a diameter of 610 m measured from LROC NAC images and a total depth of ~ 70 m, with ~ 20 m below the baseline. Horatio crater has a diameter of 380 m from LROC NAC images, is also near station 5, but does not extend below the baseline. Assuming a density contrast of $\Delta \rho = 3.2 \pm 0.2$ g/cm³, and using flat, right rectangular prisms to integrate the gravity from the topography of Camelot crater lying below the baseline, we found a contribution of 0.03 mGal to the gravity. If we extend our integration out to a larger radius of 10 km, to include most of the region of the valley that has elevations below the baseline, a maximum of 0.07 mGal is contributed to the gravity. These results suggest that the entire station 5 anomaly cannot be explained by only unmodeled surface geology.

The subsurface in the vicinity of the craters may be more brecciated and therefore less dense than the assumed density ($\Delta \rho = 3.2 \pm 0.2$ g/cm³), contributing an additional negative gravity anomaly [Soderblom *et al.*, 2015; Bierson *et al.*, 2016; Milbury *et al.*, 2015]. To model this scenario, we assumed that the brecciation extended to half the crater depth below the bottom of the crater, and half the radius of the crater beyond the rim of the crater (Figure 7). We computed the gravity contributed by this low-density structure by integrating the mass from the LROC NAC DTM at 20 m resolution using 3-D, flat-topped square prisms (equations (2) and (3)), for a range of density contrasts ($\Delta \rho$) between 1.2 and 3.2 g/cm³. The results indicate that the -6.9 ± 1.6 mGal anomaly could result from brecciated material around the crater. The density required for the brecciated material depends with the size of the brecciated region, but for the model shown in Figure 7, an average density of 1.5 ± 0.4 g/cm³ would explain the observed station 5 anomaly.

The station 5 negative anomaly could also reflect a subsurface feature that has no surface expression. For example, a lava tube would have the largest possible subsurface density contrast ($\Delta \rho = -3.2 \pm 0.2$ g/cm³). It is possible to model the lava tube as an infinite cylinder, constraining the minimum burial depth with the depth of the Camelot crater (~ 70 m), and the size-depth ratio for the lava tube by matching the amplitude of the anomaly. Additionally, the orientation of the lava tube can be roughly constrained using the location of neighboring stations. One can imagine various other subsurface features that could produce this anomaly, but given the resolution of the data, further analysis is not warranted.

4.2. Sensitivity Study

As mentioned above, even for our preferred model, there are strong discrepancies between the model and the data which are related to structure not present in our simplified physical model. For a future survey, in an optimal geologic setting, and an ideal survey architecture (i.e., with an underlying 2-D geometry, with no additional density heterogeneities, and an improved station distribution) how well can the underlying model be recovered? To determine this, we performed a sensitivity study, where we assumed an underlying 2-D geometry with $\theta = 30^\circ$, $t = 1$ km, $(W_L, W_R) = (2, 0)$ km. We then computed the gravity predicted along line T by this

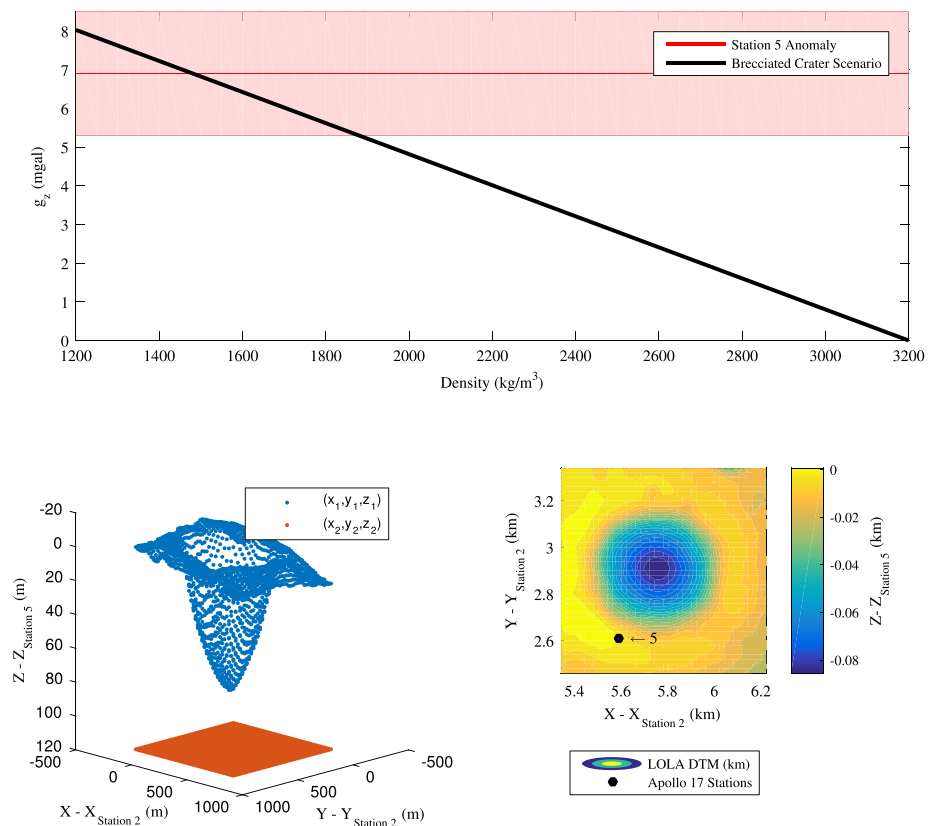


Figure 7. (a) Gravity as a function of density, generated from the brecciated crater scenario (black), assuming a brecciation extent half the crater depth below the bottom of the crater and half the radius of the crater beyond the rim of the crater. Amplitude of the station 5 anomaly is also shown (red line with uncertainties denoted by the shaded light red region). (b) Coordinates of the top and bottom integration surfaces, used in equations (2) and (3). (c) The LROC NAC DTM at 20 m resolution, cropped to the integration area.

model using dense sampling (250 measurements, i.e., ~50 m spacing), assuming no noise. Synthetic gravity data for a suite of 2-D models ($W_L = 2 \pm 2$ km, $W_R = 0$ km, $t = 1000 \pm 200$ m, and $\theta = 15$ and 90°) were computed using the same sampling density, with no noise. We computed the RMS difference between the gravity data predicted by the underlying model and the synthetic gravity data for each model in our suite of other models. Figure 8 shows the model parameter trade-offs in this best case (2-D) geological scenario. It is important to mention that Figure 8 does not show the model covariance for the TGE data and the synthetic tests result in smaller misfits than for the actual data. However, the structure of the trade-off space shown in Figure 8 is consistent with Figure 6d, as it most strongly depends on the choice of wall position, with substantially less sensitivity to all (t , θ) choices, even when the wall positions are close to their true values.

Understanding the extent of the trade-off space for a future scenario requires an estimate of the noise level for the survey. The 2.5 mGal isoline in Figure 8 shows the parameter space for models that are acceptable at the noise level of the TGE survey. For example, the wall positions can be constrained to within 1 km accuracy. In fact, noise levels can be as high as 4 mGal before the wall position is no longer resolvable within 1 km. At the 2.5 mGal TGE survey noise level, the thickness can only be constrained to within ± 150 m, and the wall angle to within $\pm 20^\circ$, assuming the fill density is well characterized. Future surveys, with lower noise levels, can better constrain the fill thickness and wall angle. For example, if one could achieve 1.0 mGal total noise, the thickness could be constrained to less than 15% of the range in values tested, approximately $t \pm 50$ m. To achieve this, the largest sources of noise need to be significantly reduced. The most important would be reducing the instrumental noise and ensuring equally spaced, higher spatial resolution measurements than the ones taken as part of the TGE. Reducing the density uncertainties would require additional density analysis on samples gathered from TLV and other similar Apollo landing sites.

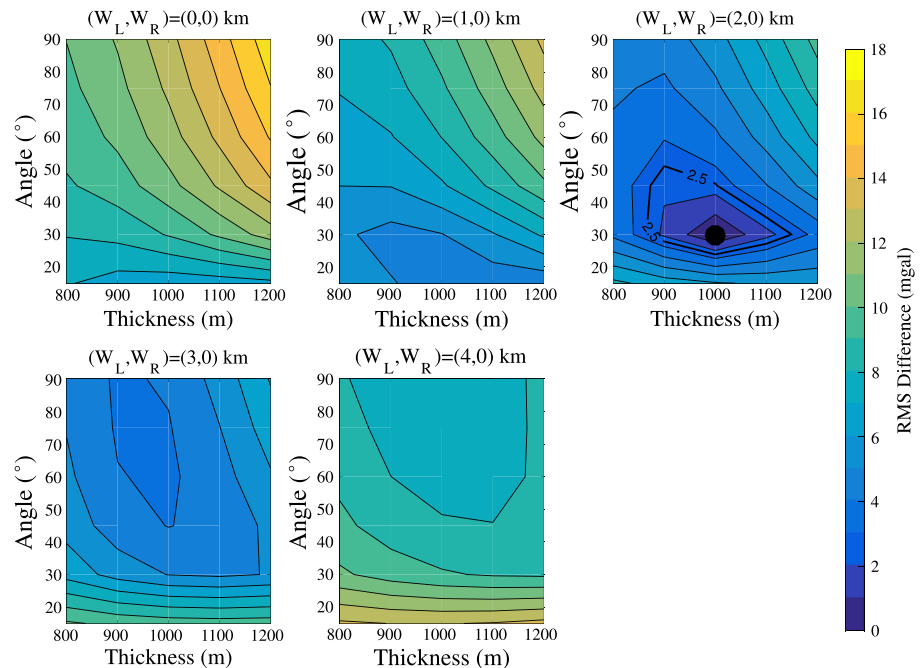


Figure 8. Contour images with 1 mGal spacing, showing RMS misfits to synthetic data between all modeling parameter combinations and the underlying 2-D model ($t = 1$ km, location $= (W_L, W_R) = (2$ km, 0 km), and a wall angle of 30°) in an ideal case with no noise. The 2.5 mGal isoline represents the total noise level from the TGE and encloses the acceptable 2-D models at that noise level.

5. Conclusions

In this study, we used an updated, high-resolution elevation model to perform 3-D corrections to the TGE data set. We found that the accuracy of individual corrections is significantly improved and the corrected data curve agrees within uncertainty with that in T73. In our modeling, we found a best fit rectangular model for the TLV fill that agrees with T73. Models for the valley with sloped walls are not well constrained, but the lowest RMS error model parameters correspond to $\theta = 30^\circ$, $t = 1$ km, and $(W_L, W_R) = (2, 0)$ km. This preferred model and the preferred model from T73 constrain the depth of volcanics extruded at TLV to be ~ 1 km.

For the preferred model, we found that there were strong trade-offs between model parameters. Particularly, we found a strong sensitivity to wall position, and substantially less sensitivity to thickness and wall angle. We found that deviations of the model from the data were sometimes large, such as the -6.9 mGal anomaly at station 5 and RMS misfit values for the preferred model (4.1 mGal) were greater than the average uncertainty in the corrected data profile (~ 2.5 mGal). This indicates that the misfit is also controlled by additional structure not accounted for in our simple models. One such case is station 5, for which tests (section 4.1) showed that a local reduction in density associated with a brecciated region around Camelot crater can reproduce the amplitude of the station 5 anomaly. It is also possible that the station 5 negative anomaly could reflect a sub-surface feature, such as a lava tube. However, testing this hypothesis would require higher sampling density around the station.

We performed a sensitivity study (section 4.2), in which we determined the parameter trade-offs in an optimal geological setting, assuming a simple 2-D valley geometry and finely and equally spaced stations. Our sensitivity study illustrated that in such an ideal case, similar parameter trade-offs to those found in modeling the TGE data occur. As for the TGE data, the wall positions exert the dominant control on model misfit. Our sensitivity study constrains the uncertainty in the model parameters at a given noise level. At the average TGE survey noise level of 2.5 mGal, the wall position can be determined within 1 km accuracy, the thickness within ± 150 m, and the wall angle to within $\pm 5^\circ$, assuming the fill density is well characterized. However, to constrain t to within a tighter range, say 15%, noise level less than 1.0 mGal is needed.

Our sensitivity study shows that to more concretely determine the geometric model for the subsurface, one would ideally like a dense array of stations (e.g., 100 m, an order of magnitude finer than in the TGE), and lower

instrumental and density uncertainties. This study also provides an estimate of the average postprocessing noise one can expect for a gravity survey similar to the A17 TGE (~2.5 mGal). These results can be used as guides for future lunar gravimetry surveys to gain the most subsurface information possible in regions with a similar subsurface geometry to TLV. Coupling our results with other future geophysical surveys, such as ground penetrating radar or shallow reflection seismic surveys, taken at TLV would allow for a deeper study of the formation of the features associated with subsurface faulting around lunar impact sites, and stronger constraints on the volume of volcanics extruded at TLV. This, in turn, would provide more information about the local geological history at, and surrounding, TLV.

Acknowledgments

This work was supported in part by Natural Sciences and Engineering Research Council of Canada (NSERC) Discovery Grants to R. Ghent and C. L. Johnson and a NSERC PGS D scholarship to N. Urbancic. Portions of this work were carried out as part of a Lunar Surface Gravity Geophysics Science Definition Study, led by Gedex Systems Inc., with funding from the Canadian Space Agency. LROC NAC, WAC, and DTM data are freely available through the RDR Products search interface through the Lunar Reconnaissance Orbiter Camera website (http://wms.lroc.asu.edu/lroc/rdr_product_select). The LROC NAC DTM used is found under the name "NAC_DTM_APOLLO17.TIF". LRO LOLA DTM for the region can be downloaded from the LOLA team Geosciences PDS website under the name "SLDEM2015_512_00N_30N_000_045.JP2" (<http://imbrium.mit.edu/DATA/SLDEM2015/GLOBAL/JP2/>). The TGE data can be found in both Table 13.1 from Talwani et al. [1973] and Table 1 from Talwani [2003]. Density values have been derived from Figure 13.8 in Talwani et al. [1973].

References

- Archinal, B. A., et al. (2011), Report of the IAU Working Group on cartographic coordinates and rotational elements, *Celestial Mech. Dyn. Astron.*, *109*(2), 101–135.
- Bierson, C. J., et al. (2016), Interactions between complex craters and the lunar crust: Analysis using GRAIL data, *J. Geophys. Res. Planets*, *121*, 1488–1497, doi:10.1002/2016JE005090.
- Fassett, C. I., and B. J. Thomson (2014), Crater degradation on the lunar maria: Topographic diffusion and the rate of erosion on the Moon, *J. Geophys. Res. Planets*, *119*, 2169–9100, doi:10.1002/2014JE004698.
- Kattoum, Y. N., and J. C. Andrews-Hanna (2013), Evidence for ring-faults around the Orientale basin on the Moon from gravity, *Icarus*, *226*(1), 694–707.
- Kreslavsky, M. A., and J. W. Head (2016), The steepest slopes on the Moon from Lunar Orbiter Laser Altimeter (LOLA) Data: Spatial distribution and correlation with geologic features, *Icarus*, *273*(15), 329–336.
- Lowrie, W. (2007), Fundamentals of geophysics.
- Lucchitta, B. K. (1977), Crater clusters and light mantle at the Apollo 17 site—A result of secondary impact from Tycho, *Icarus*, *30*(1), 80–96.
- Milbury, C., et al. (2015), Preimpact porosity controls the gravity signature of lunar craters, *Geophys. Res. Lett.*, *42*, 9711–9716, doi:10.1002/2015GL066198.
- Nagy, D. (1966), The gravitational attraction of a right rectangular prism, *Geophysics*, *31*(2), 362–371.
- Oberst, J., F. Scholten, K. D. Matz, T. Roatsch, M. Wählisch, I. Haase, P. Gläser, K. Gwinner, M. S. Robinson, and L. Team (2010), Apollo 17 landing site topography from LROC NAC stereo data—First analysis and results, in *Proceedings of the 41st Lunar and Planetary Science Conference*, LPI Contribution 1533., p. 2051, Woodlands, Tex.
- Parasnis, D. S. (1986), Principles of applied geophysics.
- Robinson, M. S., et al. (2010), Lunar Reconnaissance Orbiter Camera (LROC) instrument overview, *Space Sci. Rev.*, *150*(1–4), 81–124.
- Ryder, G., H. H. Schmitt, and P. D. Spudis (1992), Workshop on geology of Apollo 17 landing site: The Apollo 17 regolith, *LPI Tech. Rep. 92-09 Part 1*, pp. 26–27, Houston, Tex.
- Schmitt, H. H., N. E. Petro, R. A. Wells, M. S. Robinson, B. P. Weiss, and C. M. Mercer (2016), Revisiting the field geology of Taurus Littrow, *Icarus*, doi:10.1016/j.icarus.2016.11.042.
- Soderblom, J. M., et al. (2015), The fractured Moon: Production and saturation of porosity in the lunar highlands from impact cratering, *Geophys. Res. Lett.*, *42*, 6939–6944, doi:10.1002/2015GL065022.
- Talwani, M., J. L. Worzel, and M. Landisman (1959), Rapid gravity computations for two-dimensional bodies with application to the Mendocino submarine fracture zone, *J. Geophys. Res.*, *64*(1), 49–59.
- Talwani, M., G. Thompson, B. Dent, H-G. Kahle, and S. Buck (1973), Traverse Gravimeter Experiment, *Apollo 17 Preliminary Sci. Rep.*, pp. 6–34, NASA, Washington, D. C.
- Talwani, M. (2003), The Apollo 17 gravity measurements on the Moon, *The Leading Edge*, *22*(8), 786–789.
- Thatcher, W., and D. P. Hill (1991), Fault orientations in extensional and conjugate strike-slip environments and their implications, *Geology*, *19*(11), 1116–1120.
- Wolfe, E. W., N. G. Bailey, B. K. Lucchitta, W. R. Muehlberger, D. H. Scott, R. L. Sutton, H. G. Wilshire, R. M. Batson, K. B. Larson, and R. L. Tyner (1981), The geologic investigation of the Taurus-Littrow Valley; Apollo 17 landing site, with a section on Apollo 17 lunar surface photography, Prof. Pap. 1080, U.S. G.P.O., Wash.
- Zuber, M. T., et al. (2010), The Lunar Reconnaissance Orbiter Laser Ranging Investigation, *Space Sci. Rev.*, *150*(1–4), 63–80.
- Zuber, M. T., D. E. Smith, M. M. Watkins, S. W. Asmar, A. S. Konopliv, F. G. Lemoine, H. J. Melosh, G. A. Neumann, R. J. Phillips, S. C. Solomon, and M. A. Wieczorek (2013), Gravity field of the Moon from the gravity recovery and interior laboratory (GRAIL) mission, *Science*, *339*(6120), 668–671.